Biophysical Journal
Article

Biophysical Society

Disruption of Ankyrin B and Caveolin-1 Interaction Sites Alters Na^+,K^+-ATPase Membrane Diffusion

Cornelia Junghans,[1] Vladana Vukojević,[2] Neslihan N. Tavraz,[1] Eugene G. Maksimov,[3] Werner Zuschratter,[4] Franz-Josef Schmitt,[1] and Thomas Friedrich[1,*]

[1]Technical University of Berlin, Institute of Chemistry, Berlin, Germany; [2]Department of Clinical Neuroscience, Center for Molecular Medicine, Karolinska Institutet, Stockholm, Sweden; [3]Department of Biophysics, Faculty of Biology, M. V. Lomonosov Moscow State University, Moscow, Russia; and [4]Special Lab Electron and Laserscanning Microscopy, Leibniz Institute for Neurobiology, Magdeburg, Germany

ABSTRACT The Na^+,K^+-ATPase is a plasma membrane ion transporter of high physiological importance for ion homeostasis and cellular excitability in electrically active tissues. Mutations in the genes coding for Na^+,K^+-ATPase α-subunit isoforms lead to severe human pathologies including Familial Hemiplegic Migraine type 2, Alternating Hemiplegia of Childhood, Rapid-onset Dystonia Parkinsonism, or epilepsy. Many of the reported mutations lead to change- or loss-of-function effects, whereas others do not alter the functional properties, but lead to, e.g., reduced protein stability, reduced protein expression, or defective plasma membrane targeting. Na^+,K^+-ATPase frequently assembles with other membrane transporters or cellular matrix proteins in specialized plasma membrane microdomains, but the effects of these interactions on targeting or protein mobility are elusive so far. Mutation of established interaction motifs of the Na^+,K^+-ATPase with ankyrin B and caveolin-1 are expected to result in changes in plasma membrane targeting, changes of the localization pattern, and of the diffusion behavior of the enzyme. We studied the consequences of mutations in these binding sites by monitoring diffusion of eGFP-labeled Na^+,K^+-ATPase constructs in the plasma membrane of HEK293T cells by fluorescence correlation spectroscopy as well as fluorescence recovery after photobleaching or photoswitching, and observed significant differences compared to the wild-type enzyme, with synergistic effects for combinations of interaction site mutations. These measurements expand the possibilities to study the consequences of Na^+,K^+-ATPase mutations and provide information about the interaction of Na^+,K^+-ATPase α-isoforms with cellular matrix proteins, the cytoskeleton, or other membrane protein complexes.

INTRODUCTION

The Na^+,K^+-ATPase belongs to the widely distributed class of P-type ATPases (1). It converts the energy from ATP hydrolysis to electrochemical gradients of Na^+ and K^+ across the cell membrane. The enzyme transports three Na^+ ions out of and two K^+ ions into the cell for each hydrolyzed ATP molecule. The resulting ion gradients are critical for ion homeostasis, secondary active transporters, the cellular resting potential, and for enabling action potentials during neuronal signaling or muscle contraction. The pivotal importance of Na^+,K^+-ATPase (or Na^+ pump) is underlined by the fact that this enzyme can be the principal consumer of cellular ATP, especially in the central nervous system, where the Na^+ pump accounts for up to 70% of total ATP turnover.

The minimal functional unit of the Na^+,K^+-ATPase includes a large catalytic α-subunit with 10 transmembrane (TM) segments and a large cytoplasmic domain, and a smaller accessory β-subunit with one TM segment and a heavily glycosylated ectodomain (Fig. 1 *A*). Depending on the tissue, another small, single transmembrane-spanning γ-subunit is present (Fig. 1 *A*), which belongs to the class of FXYD proteins (2). The α-subunit is responsible for the catalytic activity and ion transport of the enzyme and undergoes reversible phosphorylation coupled to distinct conformational transitions that coordinate ATP hydrolysis and cation transport. The β-subunit is required for the normal activity and for the structural and functional maturation of the α-subunit. Four α- and three β-isoforms have been identified in humans, which assemble in different combinations to form Na^+,K^+-ATPase isozymes with distinct, physiologically relevant, kinetic properties (3), which are tailored or regulated in a tissue- and developmental-specific manner (see reviews in (4–6)) to adjust the isoforms' expression and activity to particular physiological requirements (7).

Since 2003, genetic research has revealed that mutations in the human genes for α_2- and α_3-isoforms cause

Submitted May 30, 2017, and accepted for publication August 14, 2017.

*Correspondence: friedrich@chem.tu-berlin.de

Editor: Ian Forster.

https://doi.org/10.1016/j.bpj.2017.08.053

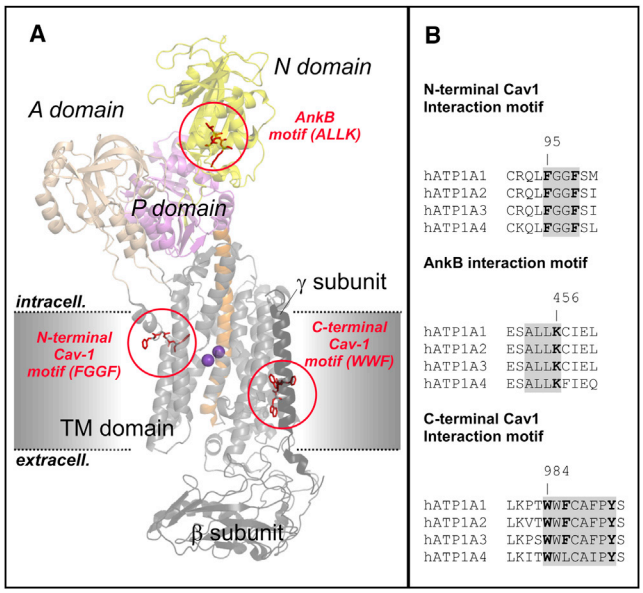

FIGURE 1 X-ray crystal structure of the Na^+,K^+-ATPase and sequence alignment of Cav-1 and AnkB interaction sites in human Na^+,K^+-ATPase α-isoforms. (*A*) Shown here is the structure of the Na^+,K^+-ATPase in the Rb^+-bound E_2 conformation (according to PDB: 2ZXE) (54). The positions of the two interaction motifs with caveolin-1 (mutated in constructs NaK-ΔC, NaK-ΔN) and one for ankyrin B (mutated in construct NaK-K456E) are encircled. The functional domains of the Na^+,K^+-ATPase are indicated by different colors (N, nucleotide binding domain; P, phosphorylation domain; A, actuator domain; TM, transmembrane domain). The location of the β- and γ-subunit is also indicated. Two spheres indicate bound Rb^+ ions as congeners for K^+. (*B*) Given here is a sequence alignment of Cav-1 and AnkB interaction motifs (highlighted in *gray*, conserved aromatic residues or Lys-456 indicated in *black*) in human Na^+,K^+-ATPase α-isoforms (numbering refers to the human α_2-subunit). To see this figure in color, go online.

severe neurological diseases including Familial Hemiplegic Migraine type 2 (FHM2) (8), Rapid-onset Dystonia Parkinsonism (9), and Alternating Hemiplegia of Childhood (10,11). The phenotypic spectra of these syndromes overlap significantly, and include cognitive, movement, and psychiatric disorders, migraines, and epilepsies. The establishment of Na^+,K^+-ATPase as a paramount target for neurological disorders has stimulated research on structure-function relationships, regulation, and pharmacological interference of this important enzyme.

Whereas most mutations identified in FHM2 (and Rapid-onset Dystonia Parkinsonism or Alternating Hemiplegia of Childhood as well) lead to distinct functional changes of the Na^+,K^+-ATPase supporting the notion of loss-of-function effects, several FHM2 mutations, in part, failed to exhibit functional alterations (12). Thus, to completely address all possible pathophysiological implications of Na^+,K^+-ATPase mutations, functional studies must not only include electrophysiological and biochemical experiments, but should also assess effects regarding protein misfolding, α/β subunit assembly, plasma membrane targeting, premature protein degradation, protein phosphorylation, and—importantly—interactions with other proteins that might interfere with the aforementioned processes (7). Two major points on this list have not been scrutinized yet regarding their impact on pathogenesis: 1) the determinants of plasma membrane targeting; and 2) the processes that are critical for the recruitment of Na^+,K^+-ATPase to distinct subdomains of the plasma membrane.

The impact of subcellular targeting of the Na^+,K^+-ATPase on its role in health and disease is still a matter of debate. It is known that Na^+,K^+-ATPase, in particular the α_2-subunit found in glial cells of the central nervous system or in cardiomyocytes, forms complexes with the Na^+,Ca^{2+} exchanger (NCX) and the inositol-1,4,5-triphosphate receptor in special Ca^{2+} signaling microdomains (13), or with NCX, the ryanodine receptor and the sarcoendoplasmic Ca^{2+}-ATPase in so-called junctional endoplasmic reticulum microdomains (14–18). Several reports indicated that the human Na^+,K^+-ATPase interacts with other cellular matrix proteins or constituents of the cytoskeleton. One such interaction partner for cellular targeting of the Na^+,K^+-ATPase is ankyrin B (13,19,20). Ankyrins are cytoskeletal scaffold proteins that contain highly adaptive, combinatorially and quasi-independently operating interaction sites to accommodate numerous target protein motifs of strikingly diverse sequences to determine the distribution of their binding targets in the cell membrane and to assemble large signaling complexes (21). Three classes of ankyrins are distinguished—ankyrin R, ankyrin G, and ankyrin B (AnkB)—with the latter being broadly expressed in most cell types. All ankyrins are composed of four functional domains, an N-terminal membrane-binding domain consisting of 24 ankyrin repeats, a central domain that binds to the cytoskeletal protein spectrin, a death domain, and a variable C-terminal regulatory domain. With its molecular mass of 440 kDa, AnkB is a particularly large representative and has an additional 220-kDa random coil domain between the spectrin and the death domain. Ankyrins B and G are required for the polar distribution of many membrane proteins, and the interaction with AnkB enables transport of the Na^+,K^+-ATPase from endoplasmic reticulum via the Golgi and stabilizes the enzyme in the plasma membrane. Importantly, mutations in the *ANK2* gene cause Long-QT syndrome type 4, a severe form of cardiac arrhythmia, by disrupting targeting of particularly the Na^+,K^+-ATPase α_2-isoform, NCX, and inositol-1,4,5-triphosphate receptor to transverse tubules and by reducing the overall protein levels. One sequence motif for interaction of the Na^+,K^+-ATPase α-subunit with AnkB has been described (19), which is conserved in all human α-isoforms (Fig. 1 *B*). This Ala-Leu-Leu-Lys motif resides in the nucleotide-binding (N) domain (Fig. 1 *A*) and comprises a positively charged lysine (Lys-456), which, upon a charge-inverting mutation, should drastically interfere with the AnkB interaction.

Another established Na^+,K^+-ATPase interaction partner is caveolin-1 (Cav1). Caveolins form the scaffold of caveolae

membrane domains, building invaginations with a typical size of 50–100 nm in the plasma membrane (22). Three different caveolin forms with tissue-specific expression and distribution in mammalian cells are known, from which Cav1 is characterized best. Cav1 has a molecular mass of 18–24 kDa, two putative TM segments, and is found mostly in the plasma membrane and in Golgi-derived vesicles. The protein forms complexes of ~13–16 monomers and is frequently coexpressed with, and interacts with, caveolin-2 (23). Many cellular functions have been associated with caveolae, and disruptions of caveolin targeting have been linked to dystrophies and defects of cellular signaling cascades or endocytosis (24,25). The Na^+,K^+-ATPase has been found to affect caveolin trafficking and stabilization of Cav1 in the plasma membrane (26,27). Two Cav1 binding motifs on the Na^+,K^+-ATPase α-subunit have been identified (27), which resemble the typical pattern $\Phi XXXX\Phi XX\Phi$ or $\Phi X\Phi XXXX\Phi$ (with Φ representing an aromatic amino acid, and X any amino acid). The N-terminal motif resides at the intracellular interface of TM segment 2 and the C-terminal motif resides at the extracellular interface of TM segment 10 (Fig. 1 *A*). Both motifs are highly conserved in human α-isoforms; only the sperm-specific α_4 has a Leu residue instead of the otherwise conserved Phe in the C-terminal motif (Fig. 1 *B*). The consequences of mutational interference with these AnkB and Cav1 binding motifs are the subject of this work, which aims to disclose whether interactions of the Na^+,K^+-ATPase α_2-isoform with these proteins influence the cellular distribution pattern or the mobility of the enzyme in the plasma membrane. Due to the conservation of these motifs, the implications most likely extend to the other human α-isoforms as well.

The mobility of proteins in living cells can be probed by fluorescence correlation spectroscopy (FCS), after the implementation of a fluorescence labeling scheme. FCS observes the fluorescence intensity fluctuations generated by molecules diffusing through a confocal volume of ~1 fL, and allows simultaneous observation of multiple diffusing molecular species without the need for their physical separation. To enable fluorescence monitoring, eGFP or the photoswitchable eGFP variant Dreiklang (DRK (28)) was fused to the N-terminus of the human Na^+,K^+-ATPase α_2-subunit. The N-terminal Cav1 binding site was disrupted by mutations F95A/F98A (construct NaK-ΔN), the C-terminal Cav1 binding motif by mutations W984A/F986A (construct NaK-ΔC), and the AnkB binding motif by mutation K456E. Furthermore, combinations of these mutations (NaK-ΔNΔC and NaK-ΔNΔCK456E) were analyzed to determine whether the effects of mutations are synergistic. Different diffusion times determined by FCS and diffusion coefficients calculated thereof provide information about the interaction of Na^+,K^+-ATPase α_2-isoform with cellular matrix proteins or membrane microdomains. As an alternative, fluorescence recovery after photobleaching (FRAP) and fluorescence recovery after photoswitching (FRAS) was applied to evaluate and compare different experimental schemes that are commonly used to target lateral diffusion of plasma membrane proteins.

MATERIALS AND METHODS

cDNA constructs

The cDNA constructs of N-terminally eGFP-tagged (or DRK-tagged) human Na^+,K^+-ATPase α_2-subunits (harboring mutations Q116R and N127D in the ouabain binding region to confer reduced ouabain sensitivity, as reported in (29)) were generated within the pcDNA3.1X vector (12) by recombinant PCR. Three groups of amino acids within reported Cav1 or AnkB interaction motifs of the Na^+,K^+-ATPase α_2-subunit were mutated using the QuikChange site-directed mutagenesis kit (Agilent, Santa Clara, CA), resulting in the following constructs: NaK-ΔN (disruption of N-terminal Cav1 binding site, mutations F95A/F98A), NaK-ΔC (disruption of C-terminal Cav1 binding motif, mutations W984A/F986A), and NaK-K456E (disruption of AnkB binding motif, mutation K456E), as well as two constructs combining sets of these mutations: NaK-ΔNΔC and NaK-ΔNΔCK456E. All cDNA constructs were verified by sequencing (Eurofins MWG Operon, Ebersberg, Germany).

Cell culture and transient transfection

Human embryonic kidney (HEK293T) cells were cultivated at 37°C in humidified 5% CO_2 atmosphere in DMEM cell culture medium with Phenol Red (Gibco/Thermo Fisher Scientific, Waltham, MA), supplemented with 5% fetal bovine serum and 1% penicillin/streptomycin. For transient transfection, 300 μL of cells per well were seeded in an eight-well Nunc Lab-Tek Chambered Cover Glass with 1.0 borosilicate bottom (Thermo Fisher Scientific). Twenty-four hours after seeding, transient transfection was performed using Lipofectamine 2000 (Invitrogen/Thermo Fisher Scientific) following the manufacturer's protocol. 18 to 24 hr after transfection, the medium was replaced by DMEM FluoroBrite (Gibco/Thermo Fisher Scientific) with 10% fetal bovine serum and 1% penicillin/streptomycin. FCS measurements were performed 36–48 h after transfection in a Phenol Red-free cell culture medium.

Confocal fluorescence microscopy and FCS

Confocal imaging, FCS measurements, and analysis of autocorrelation curves were performed as described previously (29,30) using a 510 META Laser Scanning Microscope with a ConforCor 3 system (Carl Zeiss, Oberkochen, Germany). Excitation used the 488-nm line of an Argon laser through a 40× water-immersion objective (C-Apochromat) with a numerical aperture (N.A.) of 1.2. The emitted light was collected through the objective and separated from the emission using a dichroic mirror (HFTKP 700/488). The resulting emission passed a 505-nm long-pass filter before detection by an avalanche photodiode. For imaging, the laser intensity was set to ~2% of the 15-mW maximum laser intensity. For FCS measurements, the laser intensity was set to 0.5% to avoid destruction of the sensitive biological material or photobleaching artifacts. FCS data were collected via a 70-μm pinhole in front of the avalanche photodiode detector. All experiments were carried out at 20°C.

Cellular distribution of the fluorescence-labeled Na^+,K^+-ATPase constructs was visualized by confocal laser scanning microscopy. After cell imaging, a z-scan of fluorescence intensity was performed with 0.5 μm increments over a distance of 20 μm across the cell, and FCS experiments were carried out at the upper cell membrane identified by the respective peak in fluorescence intensity.

The autocorrelation curves (ACCs) were generated from 20 × 10 s-long data series. Only ACCs from cells exhibiting a stable count rate were taken

for analysis. The measured autocorrelation curves $G(\tau)$ were normalized according to the following formula (see (29) for details):

$$Normalized\ G(\tau) = \frac{[G(\tau) - 1]}{[G(\tau_{ref}) - 1]}. \quad (1)$$

$G(\tau_{Ref})$ was calculated from the temporal average of the autocorrelation curve between $\tau = 5.2 \times 10^{-6}$ s and 4.8×10^{-5} s. All normalized autocorrelation curves were plotted, and curves deviating by more than three times the SD of the mean were discarded. Most of these deviating curves relate to bleaching processes or just showed no correlation (flat ACC curves resulting from noise).

Curve fitting used the integrated software of the ConforCor 3 system (Carl Zeiss) using the following model function for free 2D diffusion with two components and a term for triplet transitions:

$$G_{2d}(\tau) = \frac{1}{N} \cdot \underbrace{\left[\left(1 + \frac{\tau}{\tau_{D,1}}\right)^{-1} + \left(1 + \frac{\tau}{\tau_{D,2}}\right)^{-1}\right]}_{\text{Two diffusion components}} \cdot \underbrace{\left(1 + \frac{F}{1-F} \cdot e^{-k_R \cdot \tau}\right)}_{\text{triplet term}}. \quad (2)$$

The beam waist r_0 of the 488-nm laser line was calculated to be 0.17 μm based on reference measurements on rhodamine 6 G with its known diffusion coefficient in aqueous solution ($D = 2.8 \cdot 10^{-10}$ $m^2 \cdot s^{-1}$ at 22°C (31,32)). The diffusion coefficients of the different eGFP-labeled Na^+,K^+-ATPase constructs were determined by using the calibrated beam waist r_0 and the diffusion time τ_D according to the following equation:

$$D = \frac{r_0^2}{4 \cdot \tau_D}. \quad (3)$$

Two-sample Student's t-test analysis was performed to determine whether the diffusion time components of the various Na^+,K^+-ATPase constructs were significantly different ($p < 0.05$) from wild-type. The software Origin 9.1 (OriginLab, Northampton, MA) was used for data analysis and presentation.

FRAP or FRAS

Confocal image series in FRAP experiments were acquired on a TCS SP5 II microscope equipped with LAS AF acquisition software (Leica Microsystems, Wetzlar, Germany) using an 63× water immersion objective with N.A. 1.4. For image series, a continuous-wave Argon laser was used and the laser intensity was set to 25 mW of the 30 mW maximum power in the focal plane. For cells expressing DRK, the 514 nm Argon line was used for imaging (Intensity, I = 8–11%) and bleaching (I = 100%), and for eGFP-labeled samples, the 488-nm laser line was used (I = 6–10% for imaging, or 100% for bleaching). As emission range for detection, 520–600 nm was used for DRK and 500–600 nm was used for eGFP. FRAS measurements on DRK were performed using a 20× water-immersion objective with N.A. of 1.0. In this case, a Coherent Cube 405-nm diode laser (Coherent, Santa Clara, CA) of the TCS SP5 II system (I = 100%) was chosen to induce the off-switching process. All experiments were carried out at room temperature (22°C).

FRAP and FRAS image series were recorded using the FRAP Wizard of the software TCS NT (Leica) with an image size of 1024 × 128 pixels and 1400 Hz acquisition speed. First, 10 prebleach images were acquired (0.112 s time steps). Subsequently, bleaching (FRAP) or off-switching (FRAS) of a defined plasma membrane area was performed within a 5 ms bleach period at 100% laser intensity followed by acquisition of 750 postbleach images every 0.112 s (0.099 s for FRAS), followed by 100 images taken every 0.52 s using 2× line-averaging and bidirectional scanning.

FRAP/FRAS image sequences were analyzed using the software ImageJ (National Institutes of Health, Bethesda, MD) and the BioFormats plugin (https://www.openmicroscopy.org/site/support/bio-formats/users/imagej/) or the open source software easyFRAP (http://ccl.med.upatras.gr/index.php?id=easyfrap) (33). Mean fluorescence intensities $I(t)$ were calculated within a defined region of interest (ROI-1) representing the bleached membrane area. To compensate for bleaching effects over the scanning time, the averaged fluorescence intensity $I_{ref}(t)$ of a nonbleached reference membrane area (ROI-2) was determined. For background correction, the fluorescence intensity $I_{bkg}(t)$ outside the cell was determined (ROI-3). After background subtraction, a double normalization procedure was performed, which accounts for differences in starting intensities in ROI-1 and for the fluctuations of the total fluorescence signal during the experiment due to photobleaching or variations in the laser intensity:

$$I_{normalization}(t) = \left[\frac{\frac{1}{N_{pre}} \cdot \sum_{t=1}^{N_{pre}} I_{ROI-2}(t)}{I_{ROI-2}(t)}\right] \cdot \left[\frac{I_{ROI-1}(t)}{\frac{1}{N_{pre}} \cdot \sum_{t=1}^{N_{pre}} I_{ROI-1}(t)}\right]. \quad (4)$$

Here, the subscript "pre" symbolizes the prebleach image data and the time t refers to the number of the corresponding image. Subsequently, a full-scale normalization was performed according to

$$I_{FSnormalization}(t) = \frac{I_{normalization}(t) - I_{normalization}(t_{postbleach})}{1 - I_{normalization}(t_{postbleach})}, \quad (5)$$

to additionally correct for differences in the bleaching depth.

Because the normalized intensity data resulting from this analysis were not well described with a single-exponential function, a biexponential function with two characteristic times was used for fitting using a nonlinear least square minimization algorithm implemented in the software MATLAB (The MathWorks, Natick, MA):

$$I_{fit}(t) = I_0(t) - a \cdot e^{-\frac{t}{\tau_1}} - b \cdot e^{-\frac{t}{\tau_2}}. \quad (6)$$

From these fit functions, the half-recovery time $t_{1/2}$, defined as the time at which half-maximal recovery of the normalized fluorescence intensity from I_0 to I_∞ is being reached, was determined numerically for each individual cell. The half-recovery times ($t_{1/2}$) were considered as diffusion times τ_D for the calculation of diffusion constants D according to the formula described in (34), which accounts for a small bleached spot in a 2D area:

$$\tau_D = \frac{r^2 \cdot \gamma}{4 \cdot D}. \quad (7)$$

Here, r is the radius of the bleached spot, γ is introduced as a correction factor (set to 1 for full-scale normalization) for the amount of bleaching, and τ_D is the diffusion time.

Because not all bleached molecules are mobile in the plasma membrane, fluorescence recovery (intensity at infinite time after bleaching, I_∞) is usually incomplete, and the prebleach value of the fluorescence intensity I_1 will

not be reached again. The difference of I_1–I_∞ is due to immobile molecules in ROI-1, which are not replaced by intact fluorescent molecules. Thus, the fraction

$$M = \frac{I_\infty - I_0}{I_1 - I_0} \tag{8}$$

represents the mobile fraction of molecules in the observed area. Here, I_∞ indicates the normalized intensity in ROI-1 at infinite time of recovery, I_1 denotes the intensity before bleaching, and I_0 denotes the intensity just after bleaching. In the case of a full-scale normalization, the formula reduces to $M = I_\infty$. More details about experimental methods and data analysis can be found in (29,30).

Na^+,K^+-ATPase expression in *Xenopus* oocytes

Ovary material was obtained by partial ovariectomy from anesthetized *Xenopus laevis* females, and individual cells were obtained by treatment with collagenase 1A (Sigma-Aldrich, St. Louis, MO), as described (12). cRNA synthesis was carried out with the T7 mMessage mMachine kit (Ambion, Austin, TX). Each oocyte was injected with 25 ng of Na^+,K^+-ATPase α_2-subunit and 2.5 ng of human Na^+,K^+-ATPase β_1-subunit cRNAs and subsequently stored in ORI buffer (110 mM NaCl, 5 mM KCl, 1 mM $MgCl_2$, 2 mM $CaCl_2$, 5 mM HEPES, pH 7.4) containing 50 mg/L gentamycin at 18°C for 3–4 days. Preceding the experiments, intracellular [Na^+] was elevated by 45 min of incubation in Na^+-loading solution (110 mM NaCl, 2.5 mM sodium citrate, 5 mM MOPS, 5 mM Tris, pH 7.4) followed by an incubation of at least 30 min in Na buffer (100 mM NaCl, 1 mM $CaCl_2$, 5 mM $BaCl_2$, 5 mM $NiCl_2$, and 2.5 mM MOPS, 2.5 mM Tris, pH 7.4). At least two cRNA preparations of the α_2-subunit constructs and of the β_1-subunit were used for the flux experiments.

Rb^+ uptake measurements

Uptake of Rb^+ into oocytes was measured by atomic absorption spectrophotometry using an AAnalyst 800 spectrophotometer (PerkinElmer Life Sciences, Rodgau, Germany) equipped with a Rubidium hollow cathode lamp (Photron, Melbourne, Australia) and a transversely heated graphite furnace. After Na^+ loading, the oocytes were incubated for 3 min at 21–22°C in Na buffer supplemented with 1 mM RbCl and 10 μM ouabain to inhibit the endogenous Na^+,K^+-ATPase of oocytes. After three washes in Rb^+-free Na buffer and one in Milli-Q water (Millipore, Billerica, MA), individual cells were homogenized in 1 mL Milli-Q water. From these homogenates, 20-μL samples were injected into the graphite furnace for analysis using the autosampler of the atomic absorption spectrophotometry instrument. More details can be found in (35,36).

RESULTS

To clarify whether the mobility of the Na^+,K^+-ATPase in the plasma membrane of cells is dependent on known interactions with cellular matrix proteins such as AnkB or Cav1, mutant Na^+,K^+-ATPase constructs carrying an N-terminal eGFP label were generated and the diffusion behavior in the plasma membrane of HEK293T cells was analyzed by FCS.

FCS experiments

Fig. 2 shows confocal scanning fluorescence microscopy images of cells expressing the various Na^+,K^+-ATPase constructs. Compared to the cytoplasmic distribution pattern of eGFP fluorescence, all Na^+,K^+-ATPase constructs exhibited profound plasma membrane expression, as expected. Whereas the wild-type construct shows the most prominent fluorescence in the plasma membrane, in particular the fluorescence signals for NaK-K456E, the double mutant NaK-ΔCΔN, and the triple mutant NaK-ΔCΔNK456E exhibited a more diffuse pattern, with less fluorescence signal from the plasma membrane compared to intracellular fluorescence staining. This indicates that transport to the plasma membrane is already affected by these mutations.

Fig. 3 shows autocorrelation curves from FCS experiments of eGFP-labeled Na^+,K^+-ATPase constructs normalized to the same amplitude, $G(\tau) = 1$ at $\tau = 0$ μs. As described in previous work (29), the eGFP-labeled wild-type Na^+,K^+-ATPase exhibits two diffusion times (τ_1 = (533 ± 160) μs, amplitude fraction of (41 ± 6)%; and τ_2 = (63 ± 18) ms, amplitude fraction of (59 ± 6)%), from which the shorter time constant is already significantly larger than that measured for the diffusion of the isolated eGFP protein expressed in the cytoplasm ((376 ≥ 69) μs (29)).

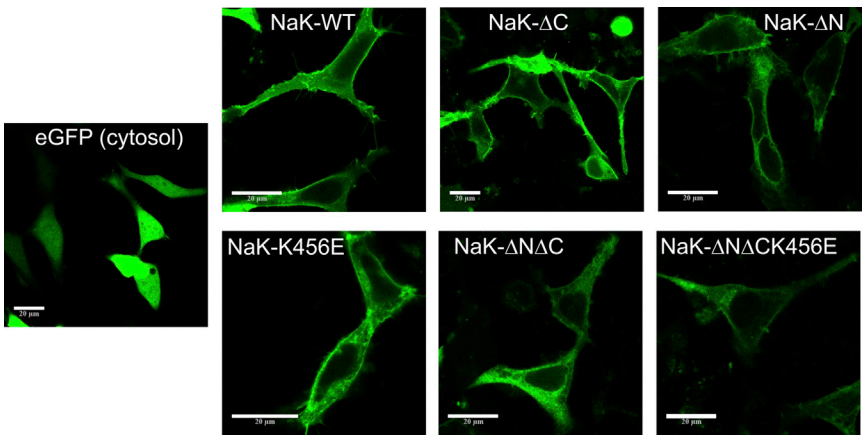

FIGURE 2 CLSM images of HEK293T cells overexpressing eGFP-labeled Na^+,K^+-ATPase constructs analyzed in this work. The different Na^+,K^+-ATPase constructs (NaK-WT, NaK-ΔN, NaK-ΔC, NaK-K456E, NaK-ΔNΔC, and NaK-ΔNΔCK456E) show typical plasma membrane localization, which is different from the distribution of eGFP expressed in the cytoplasm (*left*). Scale bars correspond to 20 μm. To see this figure in color, go online.

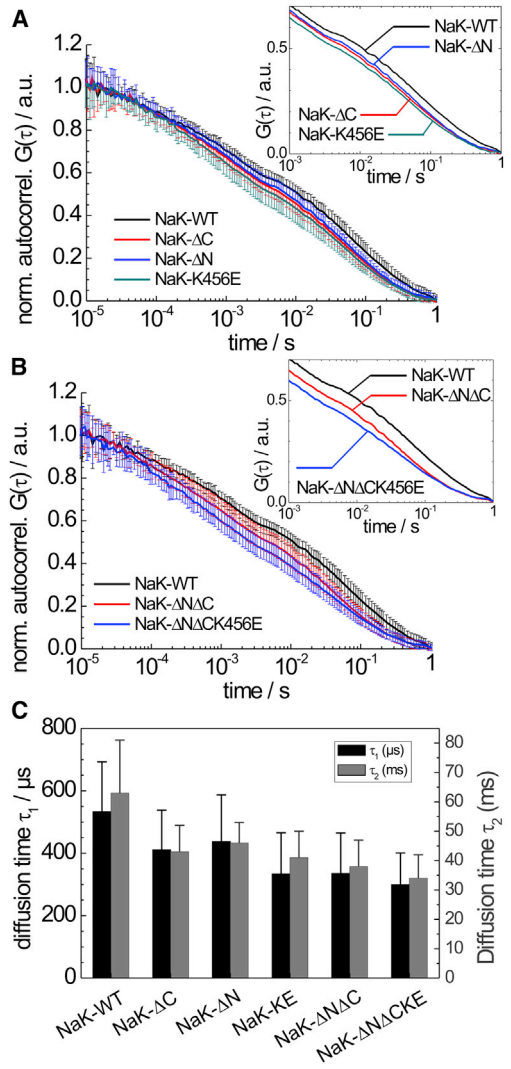

FIGURE 3 Temporal autocorrelation curves normalized to the same amplitude show differences in the lateral diffusion dynamics of different eGFP-labeled Na^+,K^+-ATPase constructs. (*A*) Given here is the comparison of NaK-WT, NaK-ΔC, NaK-ΔN, and NaK-K456E, and (*B*) the comparison of NaK-WT, NaK-ΔNΔC, and NaK-ΔNΔCK456E. Error bars correspond to SD. The insets in (*A*) and (*B*), show the autocorrelation curves without error bars in higher magnification for clarity. Data are means ± SD from 30 (NaK-WT), 31 (NaK-ΔN), 32 (NaK-ΔC), 32 (NaK-K456E), 32 (NaK-ΔNΔC), and 29 (NaK-ΔNΔCK456E) individual measurements. (*C*) Diffusion times were derived from FCS curves of (*A*) and (*B*) from fits of the model function in Eq. 2 to the datasets. Values are mean ± SD. To see this figure in color, go online.

Compared to NaK-WT, statistically different diffusion times and, consequently, diffusion constants were obtained for all Na^+,K^+-ATPase mutants, with all constructs revealing two diffusion time components (τ_1 and τ_2) with rather invariant relative amplitudes (Table 1). Of all single-motif disruptions, the AnkB-associated mutant (NaK-K456E) exhibited the fastest diffusion times, whereas the two Cav1-associated mutants (NaK-ΔN and -ΔC) showed an intermediate profile. Two-sample Student's *t*-tests confirmed that the corresponding diffusion time components of Na^+,K^+-ATPase wild-type and mutants were significantly different ($p < 0.05$).

TABLE 1 Summary of Calculated Correlation Times with Corresponding Fractional Amplitudes from FCS Experiments and the Resulting Diffusion Coefficients for the eGFP-Labeled Na^+,K^+-ATPase Constructs

Sample	Diffusion Time τ_D	Fractional Amplitude in %	Diffusion Constant D in $m^2 \cdot s^{-1}$
NaK-WT	533 ± 160 µs	41 ± 6	(1.4 ± 0.4) × 10^{-11}
	63 ± 18 ms	59 ± 6	(1.1 ± 0.3) × 10^{-13}
NaK-ΔC	411 ± 127 µs	43 ± 5	(1.8 ± 0.6) × 10^{-11}
	43 ± 9 ms	57 ± 5	(1.7 ± 0.4) × 10^{-13}
NaK-ΔN	438 ± 149 µs	42 ± 5	(1.6 ± 0.5) × 10^{-11}
	46s ± 7 ms	58 ± 5	(1.6 ± 0.2) × 10^{-13}
NaK-K456E	334 ± 132 µs	46 ± 8	(2.2 ± 0.9) × 10^{-11}
	41 ± 9 ms	54 ± 8	(1.8 ± 0.4) × 10^{-13}
NaK-ΔNΔC	335 ± 130 µs	44 ± 6	(2.2 ± 0.9) × 10^{-11}
	38 ± 9 ms	56 ± 6	(1.9 ± 0.5) × 10^{-13}
NaK-ΔNΔCK456E	299 ± 102 µs	51 ± 6	(2.4 ± 0.8) × 10^{-11}
	34 ± 8 ms	49 ± 6	(2.1 ± 0.5) × 10^{-13}

Upon combination of the Cav1-associated mutations in the double mutant NaK-ΔCΔN, the two diffusion times were faster than those from the corresponding single mutants and comparable to the results for NaK-K456E indicating that the mutations produce synergistic effects. The triple mutant NaK-ΔCΔNK456E exhibited the fastest diffusion times of all constructs investigated, which again indicates that Cav1- and AnkB-associated mutations act cooperatively. Two-sample Student's *t*-test analysis again confirmed that the corresponding diffusion time components of Na^+,K^+-ATPase wild-type and double/triple mutants were significantly different ($p < 0.001$).

From the measured diffusion times (Fig. 3 *C*), the corresponding diffusion coefficients were calculated according to Eq. 3. The calculated diffusion constants are listed in Table 1.

FRAP and FRAS experiments

Another method to characterize lateral diffusion in membranes is FRAP. To utilize fluorescence recovery as readout, we employed two experimental schemes. First, we used the standard method, in which fluorescence-labeled Na^+,K^+-ATPase molecules were bleached with intense confocal scanning illumination, which we refer to herein as "irreversible" bleaching. For this procedure, we used Na^+,K^+-ATPase constructs labeled with eGFP (as used in FCS experiments), or with the photoswitchable derivative DRK, which was the first fluorescent protein variant, for which the wavelength ranges for on- and off-switching as well as for fluorescence excitation are well separated (28). The second employed technique relied on N-terminally DRK-labeled Na^+,K^+-ATPase constructs, because

the DRK fluorophore also permits reversible off-switching by low light intensities. In principle, such an off-switching experiment with DRK could be repeated multiple times on the same cell membrane. Therefore, we refer to this scheme as "reversible" bleaching or FRAS.

Average normalized fluorescence recovery curves for fluorescence-labeled Na^+,K^+-ATPase wild-type and the Cav1- and AnkB-related mutants are shown in Fig. 4. Notably, the recovery curves acquired with the reversible FRAS scheme (Fig. 4 *A*) were characterized by much longer recovery times ($t_{1/2}$ values from exponential fits with two characteristic times; see Table 2) than the curves measured based on irreversible FRAP, irrespective of the fluorophore used (Fig. 4, *B* and *C*). This is even more striking, because recovery in irreversible FRAP should only contain contributions from nonbleached molecules diffusing into the prebleached area, whereas the reversible FRAS scheme should contain an additional contribution from slow thermal recovery of off-switched DRK molecules into the fluorescent on-state. Moreover, only in FRAS experiments, the recovery times of the Na^+,K^+-ATPase mutants were significantly ($p < 0.05$, Student's *t*-test) longer than the one of the wild-type enzyme, with the same trend among the mutants as observed in FCS experiments. In contrast, the much faster FRAP recovery curves did not show any differences between wild-type and mutants. The abnormally fast recovery curves from irreversible FRAP point at a common disadvantage of the proteinaceous GFP/DRK chromophores, which exhibit a much more complex photophysical behavior than smaller organic dye molecules, with population of dark states, triplet transitions, blinking, etc. Such problems in utilizing FPs as fluorescence tags for FRAP experiments have been described in the literature before (37) indicating that the irreversible FRAP curves rather reflect complex photophysical transitions from multiple dark states to the fluorescent state, which precludes the observation of mutation-related differences in diffusion behavior.

Thus, the FRAS scheme utilizing the DRK label indeed allows discriminating differences in the diffusion behavior of Na^+/K^+-ATPase mutants, which are qualitatively similar to FCS. As another observation, we note that the diffusion constants determined from FRAP and FRAS experiments differ from the values obtained from FCS experiments by approximately one or even two orders of magnitude. Such discrepancies between these apparently similar experimental techniques have frequently been reported in the literature, even if applied to the same molecular objects. For example, for G-protein coupled receptors, diffusion coefficients in the order of 10^{-13} $m^2 \cdot s^{-1}$ were determined by FCS and 10^{-15} $m^2 \cdot s^{-1}$ by FRAP (38). Similar effects were observed for a YFP-labeled dopamine transporter or eGFP-labeled epidermal growth factor receptor and β-adrenergic receptor (39). The authors of the latter study also showed that the resulting diffusion coefficients depend on the cell line used.

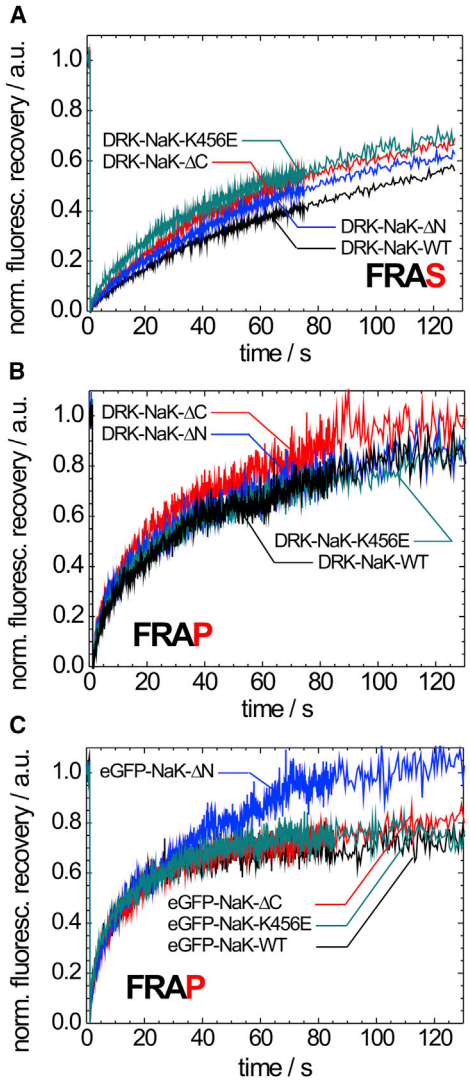

FIGURE 4 FRAS and FRAP experiments with Na^+,K^+-ATPase constructs N-terminally labeled with the photoswitchable DRK (*A* and *B*) or eGFP (*C*) upon expression in HEK293T cells. (*A*) Shown here is a reversible FRAS scheme using low-intensity off-switching of DRK by illumination with 405 nm light. Excitation used 514-nm laser light, fluorescence emission was detected in the 520–600 nm range. Data are averages from 19 (NaK-WT), 19 (NaK-ΔN), 18 (NaK-ΔC), and 19 (NaK-K456E) individual measurements. (*B*) Irreversible FRAP scheme is given, using intense illumination with 514-nm laser light to bleach DRK fluorescence. Data are averages from 16 (NaK-WT), 20 (NaK-ΔN), 20 (NaK-ΔC), and 24 (NaK-K456E) individual measurements. (*C*) Irreversible FRAP scheme is given, using intense illumination with 488-nm laser light to irreversibly bleach eGFP fluorescence. Data are averages from 20 (NaK-WT), 18 (NaK-ΔN), 19 (NaK-ΔC), and 20 (NaK-K456E) individual measurements. To see this figure in color, go online.

Activity tests by Rb^+ uptake assays on *Xenopus* oocytes

Because confocal microscopy images indicated changes in the cellular distribution of some of the Na^+,K^+-ATPase mutants, we tested whether the density of molecules in the plasma membrane was altered by the mutations. Because

TABLE 2 Summary of Determined Mobile Fractions, M; $t_{1/2}$ Values; and Calculated Diffusion Constants D for Different Na^+,K^+-ATPase Constructs from FRAS and FRAP Experiments

Sample	Method	Mobile Fraction M%	$t_{1/2}$ in s	Diffusion Constant D in m^2/s
DRK-NaK-WT	reversible (FRAS)	87 ± 17	78 ± 37	(3.2 ± 1.5) × 10^{-15}
DRK-NaK-ΔC		83 ± 22	46 ± 21	(5.4 ± 2.5) × 10^{-15}
DRK-NaK-ΔN		81 ± 19	52 ± 23	(4.8 ± 2.1) × 10^{-15}
DRK-NaK-K456E		81 ± 24	39 ± 23	(6.4 ± 3.8) × 10^{-15}
DRK-NaK-WT	irreversible (FRAP)	85 ± 18	19 ± 12	(1.3 ± 0.8) × 10^{-14}
eGFP-NaK-WT		75 ± 22	8 ± 6	(3.1 ± 2.3) × 10^{-14}
DRK-NaK-ΔC		94 ± 13	17 ± 9	(1.5 ± 0.8) × 10^{-14}
eGFP-NaK-ΔC		82 ± 19	11 ± 8	(2.3 ± 1.7) × 10^{-14}
DRK-NaK-ΔN		87 ± 15	18 ± 11	(1.4 ± 0.9) × 10^{-14}
eGFP-NaK-ΔN		93 ± 11	12 ± 5	(2.1 ± 0.9) × 10^{-14}
DRK-NaK-K456E		85 ± 17	18 ± 12	(1.4 ± 0.9) × 10^{-14}
eGFP-NaK-K456E		79 ± 19	8 ± 6	(3.1 ± 2.3) × 10^{-14}

$t_{1/2}$ represents the time of half-maximal recovery of the normalized fluorescence intensity determined from fitting the curves in Fig. 4 with Eq. 6. Mobile fractions M were determined according to Eq. 8 from the fitted curves and diffusion constants D according to Eq. 7. All values are means ± SD from the number of measurements given in the legend of Fig. 4.

the $G(0)$ value, which represents the amplitude of the autocorrelation curve at time zero, corresponds to the reciprocal of the number of molecules in the observation volume element (OVE), it can be used as a measure of the density of molecules in the plasma membrane. Fig. 5 *A* shows the average numbers of molecules in the OVE for the Na^+,K^+-ATPase constructs tested. Despite large error bars, the data by trend indicate that the NaK-K456E mutant, and even more so the double (NaK-ΔNΔC) and triple mutant (NaK-ΔNΔCK456E), are less abundant in the plasma membrane than the wild-type enzyme. To further test the functional effects of mutations, we quantified the ion-pumping function of the mutated Na^+,K^+-ATPase constructs.

To this end, the eGFP-tagged human Na^+,K^+-ATPase α_2-subunit constructs were expressed (together with human Na^+,K^+-ATPase β_1-subunit) in *Xenopus* oocytes, and pumping activity was examined by Rb^+ uptake measurements. After loading the cells with Na^+ to activate the ion pump (see Materials and Methods), cells were incubated in solution containing 1 mM RbCl for 3 min. Subsequently, the Rb^+ content of individual cells was analyzed by atomic absorption spectrophotometry using a transversely heated graphite tube furnace for atomization. Fig. 5 *B* shows Rb^+ uptake values for the various Na^+,K^+-ATPase mutants in comparison to the wild-type enzyme, whereas uninjected oocytes served as control for nonspecific Rb^+ uptake. Typical Rb^+ uptake values were ~5 pmoles (5 × 10^{-12} moles) per s per cell, which, based on a turnover number of human α_2/β_1 Na^+,K^+-ATPase of ~13 s^{-1} (12) at 22°C, corresponds to an average of 1.2 × 10^{11} pump molecules in the plasma membrane of *Xenopus* oocytes. In terms of pump current (due to the 3 Na^+: 2 K^+ transport stoichiometry, one net transported charge corresponds to two transported Rb^+ ions), 5 pmoles of Rb^+ per s per oocyte corresponds to ~200 nA pump current, which is a typical value for electrophysiological experiments on Na^+,K^+-ATPase in *Xenopus* oocytes (12) indicating that the eGFP label at the N-terminus does not alter functional activity of the wild-type enzyme. However, some of the mutants apparently exhibited lower activity. The data in Fig. 5 *B* show that the Cav1-associated mutants NaK-ΔN and -ΔC had about the same transport activity as the wild-type enzyme, but Rb^+ flux was substantially reduced for the NaK-K456E construct. The double mutant NaK-ΔNΔC showed slightly reduced Rb^+ uptake compared to wild-type, and the triple mutant NaK-ΔNΔCK456E exhibited the smallest uptake activity of all constructs tested. These observations indicate that the reduced plasma membrane localization of the NaK-K456E, NaK-ΔNΔC, and NaK-ΔNΔCK456E variants seen in CLSM images correlates, by trend, with reduced molecule density in the plasma membrane. In mutants with disrupted AnkB interaction motif (NaK-K456E, NaK-ΔNΔCK456E), the reduced transport to the plasma membrane is well reflected by reduced overall pumping activity.

DISCUSSION

In this work, the dependence of the mobility of the Na^+,K^+-ATPase α_2-subunit in the plasma membrane of HEK293T cells on the disruption of known binding motifs for Cav1 and/or AnkB was probed by FCS and FRAP/FRAS. Because the Na^+,K^+-ATPase studied here is a single entity composed of an α_2- and a β_1-subunit, one would expect only a single characteristic diffusion time. But, as outlined in previous work (29), the autocorrelation curves already for the wild-type Na^+,K^+-ATPase are complex, with two diffusion components ($\tau_1 \approx 500$ μs and $\tau_1 \approx 60$ ms) separated by two orders of magnitude corresponding to diffusion coefficients of 1.4 × 10^{-11} $m^2 \cdot s^{-1}$ and 1.1 × 10^{-13} $m^2 \cdot s^{-1}$, respectively, indicating the presence of two independent Na^+,K^+-ATPase populations with largely different mobility. Such multicomponent autocorrelation curves are not

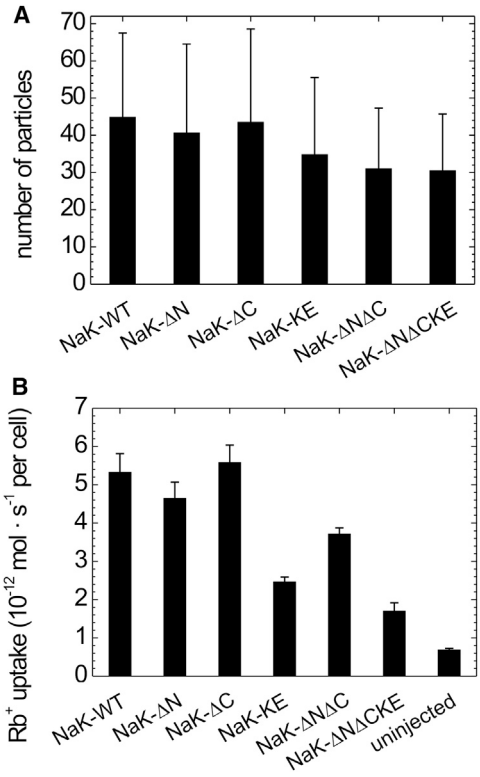

FIGURE 5 Average number of molecules in the OVE and Rb^+ uptake activity for different Na^+,K^+-ATPase constructs. (*A*) From the $G(0)$ values of the autocorrelation curves (Fig. 3, *A* and *B*), the average numbers of molecules in the observation volume element were calculated. Data are mean ± SD from 30 (NaK-WT), 29 (NaK-ΔN), 31 (NaK-ΔC), 30 (NaK-K456E), 31 (NaK-ΔNΔC), and 29 (NaK-ΔNΔCK456E) individual measurements. (*B*) Rb^+ uptake activity of the various eGFP-labeled Na^+,K^+-ATPase constructs expressed in *Xenopus* oocytes was determined by atomic absorption spectrophotometry. Data are mean ± SE; for each dataset, between 14 and 30 oocytes from the two or three independent batches measured.

uncommon for membrane proteins (40–42) and reflect the complexity of the membrane environment that allows for interactions with certain lipid domains, other membrane proteins, the cytoskeleton, or other scaffolding partners, but also exclusion from some domains. However, rationalization of either of the two diffusion components is all but straightforward.

In the literature, the diffusion time is commonly estimated from the molecular weight of a protein. The eGFP-labeled Na^+,K^+-ATPase α_2/β_1-complex has a molecular mass of ~183.5 kDa, which would result in a diffusion time of ~1.8 ms across the size of the OVE. From a rough approximation treating the diffusing molecules as spheres with hydrodynamic radii proportional to the cubic root of the molecular weight (eGFP of 26.9 kDa, eGFP-labeled Na^+,K^+-ATPase α-subunit plus glycosylated β-subunit of 183.5 kDa) the diffusion coefficient should increase by a factor of $\sqrt[3]{183.5/26.9} \approx 1.9$ for the change from isolated eGFP to eGFP-labeled Na^+,K^+-ATPase. Of course, this estimation neglects 1) that the actual shape of the molecules is different from a sphere, 2) that the Na^+,K^+-ATPase can diffuse only in two dimensions, and 3) that the dynamic viscosity of biological membranes is different from that of the cytoplasm. The fast diffusion coefficient of the eGFP-labeled Na^+,K^+-ATPase in the plasma membrane (1.4×10^{-11} $m^2 \cdot s^{-1}$) is only ~1.3-fold smaller than the diffusion time of eGFP in the cytoplasm ($D_{eGFP} = 1.9 \times 10^{-11}$ $m^2 \cdot s^{-1}$ (29)), which still agrees with the above estimation within error limits suggesting that the fast-diffusing fraction of Na^+,K^+-ATPase molecules diffuses rather freely. However, the slow diffusion component cannot be rationalized, even if one assumes that interactions of Na^+,K^+-ATPase with Cav1 macrostructures composed of 14–16 monomers (molecular mass between 300 kDa and 400 kDa (23)) are possible. Thus, formation of large hetero-oligomeric protein complexes cannot explain the extremely long diffusion times (43), and anchoring of Na^+,K^+-ATPase molecules to components of the cytoskeleton or trapping in certain membrane microdomains needs to be considered.

Literature data on Na^+/K^+-ATPase for a direct comparison is sparse and essentially stems from FRAP studies carried out decades ago. Paller (44) studied Na^+,K^+-ATPase in renal proximal tubule cells upon labeling with a fluorescent derivative of the specific inhibitor of the Na^+ pump, ouabain, and reported a diffusion constant of 3.3×10^{-14} $m^2 \cdot s^{-1}$ (at 25°C), which increased to 2.4×10^{-13} $m^2 \cdot s^{-1}$ upon treatment with cytochalasin A, an agent causing actin depolymerization and disruption of the cytoskeleton. Vaz et al. (45) studied fluorescein iodoacetamide-labeled Ca^{2+}-ATPase (~100 kDa) from rabbit muscle sarcoplasmic vesicles and reconstituted in liquid-crystalline phase bilayers, and found diffusion coefficients of 1.8×10^{-12} $m^2 \cdot s^{-1}$ (at 36°C) and 9.9×10^{-13} $m^2 \cdot s^{-1}$ (at 13°C) (45). By order of magnitude (10^{-13} $m^2 \cdot s^{-1}$), these literature FRAP data correspond to the slow diffusion constants determined by our FCS approach, but are still two orders-of-magnitude faster than the parameters determined by the reversible FRAS scheme. It should be noted that membrane protein diffusion coefficients can vary largely dependent on the cell line used, as well as for different measurement techniques (46). For other membrane-embedded proteins, recent publications list values between 10^{-16} and 10^{-14} $cm^2 \cdot s^{-1}$ (47), and a more recent FRAP study reported values between 2×10^{-14} and 2.2×10^{-13} $cm^2 \cdot s^{-1}$ depending on the number of transmembrane segments (48). However, such slow diffusion constants have not only been found for membrane proteins. Even for a farnesyl-anchored eGFP, a lateral diffusion coefficient of 5.6×10^{-13} $cm^2 \cdot s^{-1}$ in the plasma membrane of COS-7 cells was reported showing that even a fluorescent protein with a small membrane anchor can exhibit retarded diffusion, which is by two orders-of-magnitude slower than free diffusion in the cytoplasm (49).

In theory, FCS and FRAP should yield comparable information; however, there are practical differences between

FCS and FRAP, and these two methods often yield different values for the diffusion coefficient of plasma membrane-associated proteins. Whereas FCS detects the diffusion of individual molecules through an OVE of diffraction-limited size, FRAP monitors the diffusion of large ensembles of molecules into a comparatively large prebleached membrane area that is several micrometers in diameter. In addition, immobile molecules are invisible in FCS, because they do not give rise to fluorescence intensity fluctuations, but rather contribute to the background. Moreover, slowly moving molecules may be photobleached before they exit the observation volume element, giving rise to shorter decay times that can be mistaken for faster diffusion. Therefore, FCS tends to systematically overestimate diffusion coefficients. In comparison, FRAP is biased by the fact that photobleaching is not instantaneous; as photobleaching is performed, molecules enter/exit the observation volume element and the photobleached area is typically larger than the area that is specified by the ROI. As a consequence, a large pool of molecules is photobleached. In addition, subsequent (confocal) image acquisition may further suppress the fluorescence signal recovery. Hence, FRAP tends to systematically overestimate diffusion coefficients.

Super- and subdiffusion phenomena in membranes

Numerous publications suggest that membrane proteins are prone to exhibit anomalous diffusion instead of normal Brownian diffusion. In the case of anomalous diffusion, the mean-square displacement of molecules no longer scales linearly with the diffusion time τ_D, as in the case of free Brownian motion (Eq. 3). The mean-square displacement is rather proportional to ${\tau^{\alpha}}_D$, with subdiffusion characterized by $0 < \alpha \leq 1$, normal diffusion for $\alpha = 1$, and superdiffusion for $\alpha > 1$ (40,43,46,50). The complexity of the plasma membrane, with its composition of various lipids or cholesterol, with embedded membrane proteins potentially forming complexes with others or that may be linked to cytosolic and cytoskeletal proteins, creates a structural organization, which is characterized by a hierarchy of different length scales (distances determined with the precision of one order of magnitude). Due to this hierarchical patterning, also the apparent properties of diffusion phenomena depend on the length scale, across which diffusion is actually monitored. Along these lines, Wawrezinieck et al. (51) suggested that the diffusion behavior of membrane proteins must be considered as a function of the size of the OVE. On the small scale, the lipid composition gives rise to particular microdomains such as lipid rafts, in which cholesterol is tightly packed with long saturated fatty acid chains of glycosphingolipids, which in effect favors phase separation processes in the lipid bilayer to create microdomains differing largely in fluidity. On the long scale, interactions with the cellular cytoskeleton and other cellular matrix proteins, as well as integral membrane proteins, lead to the formation of a heterogeneous protein meshwork. Therefore, Wawrezinieck et al. (51) defined diffusion laws describing diffusion on different length scales. When tested regarding the existence of diffusion barriers and microdomains within the plasma membrane of COS-7 cells, the study of Lenné et al. (52) could confirm the applicability of this hierarchical method of analysis. In terms of the Na^+,K^+-ATPase studied here, the very long diffusion time component can be attributed to the dynamic patterning of biological membranes by linkage to cytoskeletal meshworks, fences, or anchoring pickets, to which the studied interactions with caveolin-1 and ankyrin B might well contribute.

The fast diffusion coefficient of the Na^+,K^+-ATPase apparently hints at superdiffusion. However, this could have trivial reasons to start with. FCS measurements on the plasma membrane always contain signal contributions from the cytoplasm, which exhibit shorter diffusion times (49,50), because in a conventional confocal setup, the length of the OVE in the axial direction is substantially larger than its radius in the plane perpendicular to the optical axis. More sophisticated explanations relate to an apparently reduced size of the observation volume element based on the microdomain model assuming that certain membrane domains are inaccessible for the diffusing species and, thus, cause artificially short diffusion times. One of the biggest challenges of FCS on plasma membranes is that the effective area that is available for diffusion is unknown. It is always assumed that the total OVE area is available for diffusion, and diffusion coefficients are calculated based on this assumption. However, such excluded spaces could be large and include cytoskeleton-anchored complexes of membrane proteins, or rigid microdomains such as lipid rafts. Also, it needs to be mentioned that, in an FCS experiment, all locally fixed fluorophores will be bleached; thus, completely immobile Na^+,K^+-ATPase molecules carrying the eGFP label will not show up in the observed fluorescence fluctuation traces, but will create inaccessible spaces that do not allow other molecules to enter. Also, the increased affinity of certain membrane proteins to special lipids may lead to accumulation in particular microdomains (40), which also biases diffusion of membrane proteins because either they cannot escape from certain microdomains (hence, diffuse slowly) or do not have access to it. In this context, the lysine-rich cluster at the N-terminus of the enzyme, which has been proposed to serve as a lipid anchor (53), could also serve in confining the mobility of the enzyme—if specific interactions to certain lipids enriched in such membrane microdomains are possible. However, such lipid anchoring would not be expected to change by the mutations in the AnkB and the Cav1 interaction sites studied here. Considerations of restricted diffusion might especially apply for caveolae, which are special lipid rafts with high cholesterol content (23). Caveolae are characterized by the presence of Cav1, a scaffolding membrane protein for which interactions

with Na^+,K^+-ATPase have been extensively discussed in the literature. Cai et al. (24) showed by FRAP measurements on LLCPK1 cells that Cav1 is highly immobile within the plasma membrane. Xie and Cai (22) assumed that enzymes like the Na^+,K^+-ATPase and other signaling proteins concentrate in caveolae to form large signaling complexes, which might well trap a certain fraction of Na^+,K^+-ATPase molecules.

CONCLUSIONS

In summary, our FCS and FRAS studies show that mutations in all previously described interaction motifs of the Na^+,K^+-ATPase with Cav1 and AnkB alter the lateral mobility of the enzyme in mammalian cell plasma membranes, and that the detected changes affect both of the observed diffusion times similarly, which indicates that disruption of the interactions are effective even on different levels of spatial organization of the plasma membrane. Moreover, the mutation in the AnkB binding site also affects the plasma membrane expression level, in line with the established role of AnkB in plasma membrane targeting of the enzyme. Due to the high conservation of the studied motifs in all human α-isoforms, these motifs can be considered as a general determinant for Na^+,K^+-ATPase scaffolding interactions and cellular localization.

Also, the effects of the individual interaction motif mutations are additive, and this synergy of effects suggests that binding sites are utilized or operated independent from each other.

Our complementary FRAP experiments showed that the use of genetically encoded chromophores is problematic due to their complex photophysics. However, the novel (to our knowledge) FRAS scheme, which exploits the reversibly photoswitchable DRK and works at much lower excitation energies, discloses qualitatively similar effects of the mutations, although the individual diffusion constants determined by FCS and FRAP/FRAS differ by one order of magnitude, which can, in part, be due to systematically inherent differences of the techniques used.

Our results set the stage for analyzing disease-related mutations of Na^+,K^+-ATPase isoforms on the level of protein dynamics and their involvement in signaling complexes or specialized membrane microdomains performing highly organized signaling functions. Future studies should focus on the mobility of disease-associated Na^+,K^+-ATPase mutations, especially if other functional tests were inconclusive. Eventually, such studies might help to establish a more comprehensive understanding of the pathophysiology of these diseases on the cellular level.

AUTHOR CONTRIBUTIONS

T.F., V.V., E.G.M., and F.-J.S. designed research. C.J. performed research. C.J., T.F., V.V., and W.Z. analyzed data, and all authors wrote the article.

ACKNOWLEDGMENTS

The authors thank Agneta Gunnar (KI Stockholm) for technical support, Dr. Marco Vitali and Prof. Rudolf Rigler for stimulating discussions, Dr. Susan Spiller for help with Rb^+ flux measurements, and Dr. Oliver Kobler (Leibnitz Institute of Neurobiology, Magdeburg) for instructions on FRAP experiments.

This work was supported by travel grants within the COST MP1205 framework (to C.J.), the Swedish Research Council (to V.V.), and the German Research Foundation, Cluster of Excellence "Unifying Concepts in Catalysis" (to T.F.).

REFERENCES

1. Axelsen, K. B., and M. G. Palmgren. 1998. Evolution of substrate specificities in the P-type ATPase superfamily. *J. Mol. Evol.* 46:84–101.
2. Sweadner, K. J., and E. Rael. 2000. The FXYD gene family of small ion transport regulators or channels: cDNA sequence, protein signature sequence, and expression. *Genomics.* 68:41–56.
3. Crambert, G., U. Hasler, …, K. Geering. 2000. Transport and pharmacological properties of nine different human Na, K-ATPase isozymes. *J. Biol. Chem.* 275:1976–1986.
4. Jørgensen, P. L., K. O. Hakansson, and S. J. Karlish. 2003. Structure and mechanism of Na,K-ATPase: functional sites and their interactions. *Annu. Rev. Physiol.* 65:817–849.
5. Kaplan, J. H. 2002. Biochemistry of Na,K-ATPase. *Annu. Rev. Biochem.* 71:511–535.
6. Shattock, M. J., M. Ottolia, …, Z.-J. Xie. 2015. Na^+/Ca^{2+} exchange and Na^+/K^+-ATPase in the heart. *J. Physiol.* 593:1361–1382.
7. Friedrich, T., N. N. Tavraz, and C. Junghans. 2016. ATP1A2 mutations in migraine: seeing through the facets of an ion pump onto the neurobiology of disease. *Front. Physiol.* 7:239.
8. De Fusco, M., R. Marconi, …, G. Casari. 2003. Haploinsufficiency of ATP1A2 encoding the Na^+/K^+ pump α2 subunit associated with familial hemiplegic migraine type 2. *Nat. Genet.* 33:192–196.
9. de Carvalho Aguiar, P., K. J. Sweadner, …, L. J. Ozelius. 2004. Mutations in the Na^+/K^+ -ATPase α3 gene *ATP1A3* are associated with rapid-onset dystonia Parkinsonism. *Neuron.* 43:169–175.
10. Heinzen, E. L., K. J. Swoboda, …, D. B. Goldstein; European Alternating Hemiplegia of Childhood (AHC) Genetics Consortium; Biobanca e Registro Clinico per l'Emiplegia Alternante (I.B.AHC) Consortium; European Network for Research on Alternating Hemiplegia (ENRAH) for Small and Medium-sized Enterpriese (SMEs) Consortium. 2012. De novo mutations in *ATP1A3* cause alternating hemiplegia of childhood. *Nat. Genet.* 44:1030–1034.
11. Rosewich, H., H. Thiele, …, J. Gärtner. 2012. Heterozygous *de-novo* mutations in ATP1A3 in patients with alternating hemiplegia of childhood: a whole-exome sequencing gene-identification study. *Lancet Neurol.* 11:764–773.
12. Tavraz, N. N., T. Friedrich, …, M. Dichgans. 2008. Diverse functional consequences of mutations in the Na^+/K^+-ATPase α2-subunit causing familial hemiplegic migraine type 2. *J. Biol. Chem.* 283:31097–31106.
13. Liu, X., Z. Spicarová, …, A. Aperia. 2008. Ankyrin B modulates the function of Na,K-ATPase/inositol 1,4,5-trisphosphate receptor signaling microdomain. *J. Biol. Chem.* 283:11461–11468.
14. Blaustein, M. P., M. Juhaszova, and V. A. Golovina. 1998. The cellular mechanism of action of cardiotonic steroids: a new hypothesis. *Clin. Exp. Hypertens.* 20:691–703.
15. Juhaszova, M., and M. P. Blaustein. 1997. Na^+ pump low and high ouabain affinity α subunit isoforms are differently distributed in cells. *Proc. Natl. Acad. Sci. USA.* 94:1800–1805.
16. Lencesova, L., A. O'Neill, …, M. P. Blaustein. 2004. Plasma membrane-cytoskeleton-endoplasmic reticulum complexes in neurons and astrocytes. *J. Biol. Chem.* 279:2885–2893.

17. Mohler, P. J., J. Q. Davis, and V. Bennett. 2005. Ankyrin-B coordinates the Na/K ATPase, Na/Ca exchanger, and InsP3 receptor in a cardiac T-tubule/SR microdomain. *PLoS Biol.* 3:e423.
18. Stabach, P. R., P. Devarajan, …, J. S. Morrow. 2008. Ankyrin facilitates intracellular trafficking of α_1-Na^+-K^+-ATPase in polarized cells. *Am. J. Physiol. Cell Physiol.* 295:C1202–C1214.
19. Jordan, C., B. Püschel, …, D. Drenckhahn. 1995. Identification of a binding motif for ankyrin on the α-subunit of Na^+,K^+-ATPase. *J. Biol. Chem.* 270:29971–29975.
20. Zhang, Z., P. Devarajan, …, J. S. Morrow. 1998. Structure of the ankyrin-binding domain of α-Na,K-ATPase. *J. Biol. Chem.* 273:18681–18684.
21. Wang, C., Z. Wei, …, M. Zhang. 2014. Structural basis of diverse membrane target recognitions by ankyrins. *eLife.* 3:e04353.
22. Xie, Z., and T. Cai. 2003. Na^+-K^+-ATPase-mediated signal transduction: from protein interaction to cellular function. *Mol. Interv.* 3:157–168.
23. Williams, T. M., and M. P. Lisanti. 2004. The Caveolin genes: from cell biology to medicine. *Ann. Med.* 36:584–595.
24. Cai, T., H. Wang, …, Z. J. Xie. 2008. Regulation of caveolin-1 membrane trafficking by the Na/K-ATPase. *J. Cell Biol.* 182:1153–1169.
25. Liu, P., M. Rudick, and R. G. W. Anderson. 2002. Multiple functions of caveolin-1. *J. Biol. Chem.* 277:41295–41298.
26. Liu, L., K. Mohammadi, …, A. Askari. 2003. Role of caveolae in signal-transducing function of cardiac Na^+/K^+-ATPase. *Am. J. Physiol. Cell Physiol.* 284:C1550–C1560.
27. Wang, H., M. Haas, …, Z. Xie. 2004. Ouabain assembles signaling cascades through the caveolar Na^+/K^+-ATPase. *J. Biol. Chem.* 279:17250–17259.
28. Brakemann, T., A. C. Stiel, …, S. Jakobs. 2011. A reversibly photoswitchable GFP-like protein with fluorescence excitation decoupled from switching. *Nat. Biotechnol.* 29:942–947.
29. Junghans, C., F.-J. Schmitt, …, T. Friedrich. 2015. Monitoring the diffusion behavior of Na,K-ATPase by fluorescence correlation spectroscopy (FCS) upon fluorescence labelling with eGFP or Dreiklang. *Optofluid. Microfluid. Nanofluid.* 2:1–14.
30. Junghans, C. 2016. Investigations on the mobility of the Na,K-ATPase in cell membranes probed by fluorescence microscopy. Dissertation. Technical University of Berlin, Berlin, Germany. 167. https://doi.org/10.14279/depositonce-5442.
31. Magde, D., E. L. Elson, and W. W. Webb. 1974. Fluorescence correlation spectroscopy. II. An experimental realization. *Biopolymers.* 13:29–61.
32. Rigler, R., P. Grasselli, and M. Ehrenberg. 1979. Fluorescence correlation spectroscopy and application to the study of Brownian motion of biopolymers. *Phys. Scr.* 19:486–490.
33. Rapsomaniki, M. A., P. Kotsantis, …, Z. Lygerou. 2012. easyFRAP: an interactive, easy-to-use tool for qualitative and quantitative analysis of FRAP data. *Bioinformatics.* 28:1800–1801.
34. Axelrod, D., D. E. Koppel, …, W. W. Webb. 1976. Mobility measurement by analysis of fluorescence photobleaching recovery kinetics. *Biophys. J.* 16:1055–1069.
35. Dürr, K. L., N. N. Tavraz, …, T. Friedrich. 2013. Measuring cation transport by Na,K- and H,K-ATPase in *Xenopus* oocytes by atomic absorption spectrophotometry: an alternative to radioisotope assays. *J. Vis. Exp.* e50201.
36. Friedrich, T. 2015. Cation uptake studies with atomic absorption spectrophotometry (AAS). *In* Pumps, Channels, and Transporters. R. J. Clarke and M. A. A. Khalid, eds. John Wiley & Sons, Hoboken, NJ.
37. Sinnecker, D., P. Voigt, …, M. Schaefer. 2005. Reversible photobleaching of enhanced green fluorescent proteins. *Biochemistry.* 44:7085–7094.
38. Calizo, R. C., and S. Scarlata. 2013. Discrepancy between fluorescence correlation spectroscopy and fluorescence recovery after photobleaching diffusion measurements of G-protein-coupled receptors. *Anal. Biochem.* 440:40–48.
39. Adkins, E. M., D. J. Samuvel, …, U. Gether. 2007. Membrane mobility and microdomain association of the dopamine transporter studied with fluorescence correlation spectroscopy and fluorescence recovery after photobleaching. *Biochemistry.* 46:10484–10497.
40. Chiantia, S., J. Ries, and P. Schwille. 2009. Fluorescence correlation spectroscopy in membrane structure elucidation. *Biochim. Biophys. Acta.* 1788:225–233.
41. Schwille, P., J. Korlach, and W. W. Webb. 1999. Fluorescence correlation spectroscopy with single-molecule sensitivity on cell and model membranes. *Cytometry.* 36:176–182.
42. Vukojević, V., Y. Ming, …, L. Terenius. 2008. μ-opioid receptor activation in live cells. *FASEB J.* 22:3537–3548.
43. Elson, E. L. 2001. Fluorescence correlation spectroscopy measures molecular transport in cells. *Traffic.* 2:789–796.
44. Paller, M. S. 1994. Lateral mobility of Na,K-ATPase and membrane lipids in renal cells. Importance of cytoskeletal integrity. *J. Membr. Biol.* 142:127–135.
45. Vaz, W. L., M. Criado, …, T. M. Jovin. 1982. Size dependence of the translational diffusion of large integral membrane proteins in liquid-crystalline phase lipid bilayers. A study using fluorescence recovery after photobleaching. *Biochemistry.* 21:5608–5612.
46. Feder, T. J., I. Brust-Mascher, …, W. W. Webb. 1996. Constrained diffusion or immobile fraction on cell surfaces: a new interpretation. *Biophys. J.* 70:2767–2773.
47. Kühn, T., T. O. Ihalainen, …, J. Timonen. 2011. Protein diffusion in mammalian cell cytoplasm. *PLoS One.* 6:e22962.
48. Kumar, M., M. S. Mommer, and V. Sourjik. 2010. Mobility of cytoplasmic, membrane, and DNA-binding proteins in *Escherichia coli*. *Biophys. J.* 98:552–559.
49. Ohsugi, Y., K. Saito, …, M. Kinjo. 2006. Lateral mobility of membrane-binding proteins in living cells measured by total internal reflection fluorescence correlation spectroscopy. *Biophys. J.* 91:3456–3464.
50. Schwille, P., U. Haupts, …, W. W. Webb. 1999. Molecular dynamics in living cells observed by fluorescence correlation spectroscopy with one- and two-photon excitation. *Biophys. J.* 77:2251–2265.
51. Wawrezinieck, L., H. Rigneault, …, P.-F. Lenné. 2005. Fluorescence correlation spectroscopy diffusion laws to probe the submicron cell membrane organization. *Biophys. J.* 89:4029–4042.
52. Lenné, P.-F., L. Wawrezinieck, …, D. Marguet. 2006. Dynamic molecular confinement in the plasma membrane by microdomains and the cytoskeleton meshwork. *EMBO J.* 25:3245–3256.
53. Jiang, Q., A. Garcia, …, R. J. Clarke. 2017. Electrostatic stabilization plays a central role in autoinhibitory regulation of the Na^+,K^+-ATPase. *Biophys. J.* 112:288–299.
54. Shinoda, T., H. Ogawa, …, C. Toyoshima. 2009. Crystal structure of the sodium-potassium pump at 2.4 Å resolution. *Nature.* 459:446–450.